Journal of Advanced Ceramics
2021, **10**(4): 0–0
https://doi.org/10.1007/s40145-021-0481-2
ISSN 2226-4108
CN 10-1154/TQ

Research Article

Growth of single crystals in the $(Na_{1/2}Bi_{1/2})TiO_3$–$(Sr_{1-x}Ca_x)TiO_3$ system by solid state crystal growth

Phan Gia LE[a], Huyen Tran TRAN[a], Jong-Sook LEE[a], John G. FISHER[a,*], Hwang-Pill KIM[b], Wook JO[b], Won-Jin MOON[c]

[a]*School of Materials Science and Engineering, Chonnam National University, 77 Yongbong-ro, Buk-gu, Gwangju 61186, Republic of Korea*
[b]*School of Materials Science and Engineering, Ulsan National Institute of Science and Technology, 50 UNIST-gil, Eonyang-eup, Ulju-gun, Ulsan 44919, Republic of Korea*
[c]*Korea Basic Science Institute, Gwangju Center, 77 Yongbong-ro, Buk-gu, Gwangju 61186, Republic of Korea*

Received: January 13, 2021; Revised: April 7, 2021; Accepted: April 9, 2021

Abstract: Ceramics based on $(Na_{1/2}B_{1/2})TiO_3$ are promising candidates for actuator applications because of large strains generated by an electric field-induced phase transition. For example, the $(1–x)(Na_{1/2}Bi_{1/2})TiO_3–xSrTiO_3$ system exhibits a morphotropic phase boundary at x = 0.2–0.3, leading to high values of inverse piezoelectric constant d^*_{33}, which can be further improved by the use of single crystals. In our previous work, single crystals of $(Na_{1/2}B_{1/2})TiO_3–SrTiO_3$ and $(Na_{1/2}B_{1/2})TiO_3–CaTiO_3$ were grown by the solid state crystal growth technique. Growth in the $(Na_{1/2}B_{1/2})TiO_3–SrTiO_3$ system was sluggish whereas the $(Na_{1/2}B_{1/2})TiO_3–CaTiO_3$ single crystals grew well. In the present work, $0.8(Na_{1/2}Bi_{1/2})TiO_3–0.2(Sr_{1-x}Ca_x)TiO_3$ single crystals (with x = 0.0, 0.1, 0.2, 0.3, 0.4) were produced by the solid state crystal growth technique in an attempt to improve crystal growth rate. The dependence of mean matrix grain size, single crystal growth distance, and electrical properties on the Ca concentration was investigated in detail. These investigations indicated that at x = 0.3 the matrix grain growth was suppressed and the driving force for single crystal growth was enhanced. Replacing Sr with Ca increased the shoulder temperature T_s and temperature of maximum relative permittivity T_{max}, causing a decrease in inverse piezoelectric properties and a change from normal to incipient ferroelectric behavior.

Keywords: $(Na_{1/2}Bi_{1/2})TiO_3$; lead-free piezoelectric; single crystal; microstructure; electrical properties

1 Introduction

Restrictions introduced by the European Union and several countries on the use of lead in electronic equipment have triggered research efforts to identify lead-free piezoelectric materials that can replace lead zirconate titanate (PZT) [1,2]. $(Na_{1/2}Bi_{1/2})TiO_3$ (NBT)-based solid solutions are well known as promising candidates for lead-free piezoelectric ceramics to replace PZT [1,3]. In the $(1–x)(Na_{1/2}Bi_{1/2})TiO_3–xSrTiO_3$ (NBT–ST) system, a morphotropic phase boundary (MPB) between rhombohedral and pseudocubic phases

* Corresponding author.
E-mail: johnfisher@jnu.ac.kr

was discovered at x = 0.2–0.3 [4,5]. The inverse piezoelectric properties at compositions near the MPB were greatly improved due to the presence of a reversible electric field-induced transition between relaxor and ferroelectric phases [4,6]. Although at compositions near the MPB, the electrical properties of the materials were significantly improved, and a shifting of the depolarization temperature T_d as well as the rhombohedral–tetragonal phase transition temperature $T_{R\text{-}T}$ to lower temperatures was also recognized. This creates a limitation in the temperature operating range of NBT–ST materials, much affecting their practical application [6].

In previous work, single crystals of $0.8(Na_{1/2}Bi_{1/2})TiO_3$–$0.2SrTiO_3$ and $0.96(Na_{1/2}Bi_{1/2})TiO_3$–$0.04CaTiO_3$ were grown by the solid state single crystal growth method [7,8]. Single crystal growth in the $0.8(Na_{1/2}Bi_{1/2})TiO_3$–$0.2SrTiO_3$ system was limited whereas the $0.96(Na_{1/2}Bi_{1/2})TiO_3$–$0.04CaTiO_3$ single crystals grew well. Matrix grain growth behaviour is an important factor in solid state crystal growth, as the driving force for single crystal growth is inversely proportionate to the mean matrix grain size [9]. Numerous works have noted the effect of composition change, dopant, or sintering aid addition on grain growth behaviour in NBT-based ceramics [10–12], but less work has been done on the effect of composition on solid state single crystal growth behaviour [13–15]. Changing the composition also has an effect on the electrical properties of NBT. For example, doping $(Na_{1/2}Bi_{1/2})TiO_3$–$BaTiO_3$ with Nb causes a decrease in grain size from 2.3 to 1.8 μm, a reduction in the peak value of relative permittivity, slimmer polarization–electric field hysteresis loops, and a change of the strain–electric field curves from butterfly- to sprout-shaped [16]. La addition to $(Na_{1/2}Bi_{1/2})TiO_3$–$BaTiO_3$ resulted in a gradual decrease of grain size, an increase in the temperature of maximum relative permittivity T_m, a decrease in room temperature relative permittivity, and decreasing ferroelectric properties [17]. Substitution of $(Na_{1/2}Bi_{1/2})TiO_3$ with $BaTiO_3$ was found to enhance the inverse piezoelectric properties of $0.8(Na_{1/2}Bi_{1/2})TiO_3$–$0.2SrTiO_3$ [18]. By changing the composition, it may be possible to grow larger single crystals of $0.8(Na_{1/2}Bi_{1/2})TiO_3$–$0.2SrTiO_3$ by repressing matrix grain growth as well as altering the electrical properties of the single crystal. In the present work Ca is substituted for Sr in $0.8(Na_{1/2}Bi_{1/2})TiO_3$–$0.2SrTiO_3$ in order to study the effects on single crystal growth behaviour and electrical properties.

2 Materials and method

Powders of composition $0.8(Na_{1/2}Bi_{1/2})TiO_3$–$0.2(Sr_{1-x}Ca_x)TiO_3$ with x = 0.0, 0.1, 0.2, 0.3, 0.4 (labelled x = 0.0 to x = 0.4) were synthesized from Na_2CO_3 (ACROS Organics, 99.5%), Bi_2O_3 (Alfa Aesar, 99.9%), TiO_2 (Alfa Aesar, 99.8%), $SrCO_3$ (Aldrich, ≥ 99.9%), and $CaCO_3$ (Aldrich, ≥ 99.9%) starting materials by solid state reaction. To prepare each powder, the starting materials were dried in an oven at 250 ℃ for 5 h to remove adsorbed water. The stoichiometrically weighed amounts of these starting materials were mixed and ground in high-purity (99.9%) ethanol in a ZrO_2-lined jar in a planetary ball mill (Planetary Micro Mill Pulverisette 7, Fritsch GmbH, Idar-Oberstein, Germany) for 3 h (with alternating 5 min milling and 1 min rest intervals) at 500 rpm using ZrO_2 media. After milling, most of the ethanol was evaporated using a hot plate and magnetic stirrer. Then, the slurry was dried in an oven at 80 ℃ for 12 h to totally remove any remaining ethanol. The dried slurry was ground in an agate mortar and pestle and sieved through a 180 μm sieve to remove agglomerates. Each powder was put into high-purity alumina double crucibles with lids and calcined at 800 ℃ for 5 h in air, with heating and cooling rates of 5 ℃/min. The calcined powders were analyzed by X-ray diffraction (XRD, X'Pert PRO, PANalytical, Almelo, the Netherlands) using Cu Kα radiation, with a scan range of 20°–90° 2θ and a scan speed of 3 (°)/min. The calcined powders were planetary ball milled, ground, and sieved again to break up any agglomerates and reduce the particle size. Particle size analysis of the powders was carried out using SEM micrographs. Transmission electron microscopy (TEM) analysis was carried out on powders with x = 0.0 and x = 0.4 in a transmission electron microscope (FEI TECNAI F 20, FEI Comp., Hillsboro, OR, USA) operated at an accelerating voltage of 200 kV. Powders were dispersed in ethanol and suspended on a porous grid.

To prepare samples of each composition by solid state crystal growth, $SrTiO_3$ single crystal seeds (MTI Corp., CA, USA) with (001) orientation and dimensions of 5 mm × 5 mm × 0.5 mm were buried in 0.5 g of prepared powder of the appropriate composition in a 10 mm steel die and pressed by hand into pellets of 10 mm diameter and ~4 mm thickness. Then the pellets were pressed in a cold isostatic press (CIP) at 1500 kg/cm (~147 MPa). To reduce evaporation of Bi and Na, CIPed pellets were buried in packing powder of

identical composition in double alumina crucibles with lids. Samples were then sintered at 1200 ℃ for 1, 3, 10, and 20 h with heating and cooling rates of 5 ℃/min. The sintered samples were vertically sectioned using a low speed diamond wheel saw, polished to a 1 μm finish with diamond paste, and thermally etched at 1150 ℃. The etched samples were Pt-coated and observed by scanning electron microscopy (SEM, Hitachi S-4700, Tokyo, Japan) with attached energy dispersive X-ray spectrometer (EDS, EMAX energy EX-200, Horiba, Kyoto, Japan). The single crystal growth distance, mean matrix grain size, and matrix grain size distribution are analyzed from the SEM micrographs using imageJ v1.50a image analysis software (National Institute of Mental Health, Bethesda, MD, USA). To analyze single crystal thickness, the single crystal in each micrograph is divided into slices and the area of each slice is measured. By dividing the area of each slice by its width, the average growth distance of the crystal in that slice could be measured. For each sample, the mean and standard deviation of 50 slices are measured. To analyze the mean matrix grain size and grain size distribution, the equivalent 2D radii of at least 200 grains are analyzed for each sample.

The thickness of single crystals grown on (001) $SrTiO_3$ seed crystals was not sufficient to separate them from the surrounding matrix grains and prepare samples for electrical property measurement. So in order to study crystal structure, dielectric, ferroelectric, and piezoelectric properties, a set of single crystals were grown by solid state crystal growth on (110) $SrTiO_3$ seed crystals (MTI Corp., CA, USA) at 1200 ℃ for 50 h. For crystal structure study, polycrystalline samples (i.e., without seed crystals) were sintered at 1200 ℃ for 1 h, crushed, and analyzed by powder X-ray diffraction (XRD, X'Pert PRO, PANalytical, Almelo, the Netherlands) using Cu Kα radiation, a 2θ scan range 20°–90°, step size 0.013°, and a scan speed 3 (°)/min. Single crystal samples grown on (110) $SrTiO_3$ seed crystals at 1200 ℃ for 50 h were separated from the surrounding matrix grains and polished with SiC paper up to grade #4000 until the (110) faces of the $0.8(Na_{1/2}Bi_{1/2})TiO_3$–$0.2(Sr_{1-x}Ca_x)TiO_3$ single crystal were exposed on both sides,i.e., the $SrTiO_3$ seed crystal as well as the matrix grains were removed, leaving behind only the $0.8(Na_{1/2}Bi_{1/2})TiO_3$–$0.2(Sr_{1-x}Ca_x)TiO_3$ single crystal. XRD was then carried out as before. For the impedance spectroscopy measurements, single crystal samples were separated from the surrounding matrix grains and were polished with SiC paper up to grade #2000 until $0.8(Na_{1/2}Bi_{1/2})TiO_3$–$0.2(Sr_{1-x}Ca_x)TiO_3$ single crystal faces with (110) orientation were exposed on both sides as above. Sample width for these samples varied from 2.5 to 4.5 mm. Sample thickness varied from 288 to 410 μm, except for the x = 0.1 sample whose thickness was only 83 μm. Both sides of each sample were then coated with Pt-paste and the sample was annealed at 900 ℃ for 30 min with heating and cooling rates of 5 ℃/min to prepare Pt electrodes. An impedance analyser (HP4284A, Hewlett-Packard, Kobe, Japan) was used to record the conductance and resistance of each sample at different temperatures and frequencies. Samples were measured in a hot stage (TS1500, Linkam, Tadworth, UK) in the temperature range of 30–780 ℃ in dry air with heating and cooling rates of 1 ℃/min. The AC voltage is set at 0.5 V and the frequency range from 1 MHz to 1 kHz. The data was processed using Origin 9.2 software (OriginLab Corporation, Northampton, MA, USA). The same single crystal samples were used for polarization and strain hysteresis measurements. For polarization and strain hysteresis measurements, the external electric field (E) dependencies of polarization (P) and strain (S) hysteresis were measured at room temperature in a commercial apparatus, aixPES (aixACCT systems GmbH, Aachen, Germany) using a bipolar electric field profile at 1 Hz. The samples were annealed at 200 ℃ for 5 min before measurement. The single crystal samples used for polarization and strain hysteresis measurements are shown in Fig. 12.

3 Results

XRD patterns of the calcined powders are shown in Fig. 1. Pattern smoothing, background, and $K\alpha_2$ peak removal were carried out using MDI Jade 6.5 (Materials Data Inc., CA, USA). All of the patterns are single phase perovskite and can be indexed to ICDD Card # 89-3109, cubic $(Na_{1/2}Bi_{1/2})TiO_3$, $Pm\bar{3}m$ space group. XRD patterns of the polycrystalline samples sintered at 1200 ℃ for 1 h are shown in Fig. 2(a). The polycrystalline samples also appear to be single phase perovskite without any secondary phase. All peaks were indexed using pseudocubic indices. The $0.8(Na_{1/2}Bi_{1/2})TiO_3$–$0.2(Sr_{1-x}Ca_x)TiO_3$ single crystal samples grown on (110) $SrTiO_3$ seed crystals at 1200 ℃ for 50 h show (110) and (220) peaks of strong intensity, confirming their single crystal nature (Fig. 2(b)). Rietveld refinement of the XRD pattern for

the x = 0.0 polycrystalline sample is shown in Fig. 3. The pattern was fitted with rhombohedral $R3c$ and cubic $Pm\bar{3}m$ phases. Rietveld refinement results of the XRD patterns of the polycrystalline samples are given in Table 1. As x increases, the amount of rhombohedral phase increases.

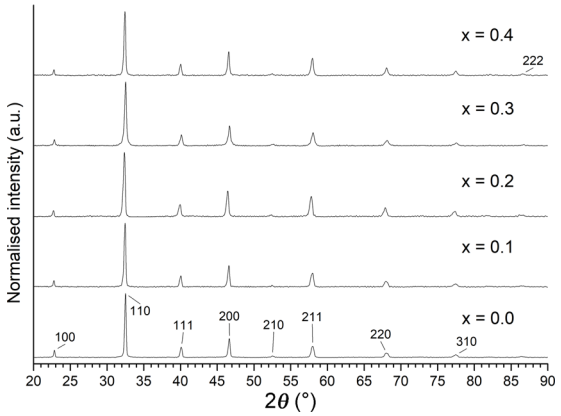

Fig. 1 XRD patterns of calcined $0.8(Na_{1/2}Bi_{1/2})TiO_3$–$0.2(Sr_{1-x}Ca_x)TiO_3$ powders.

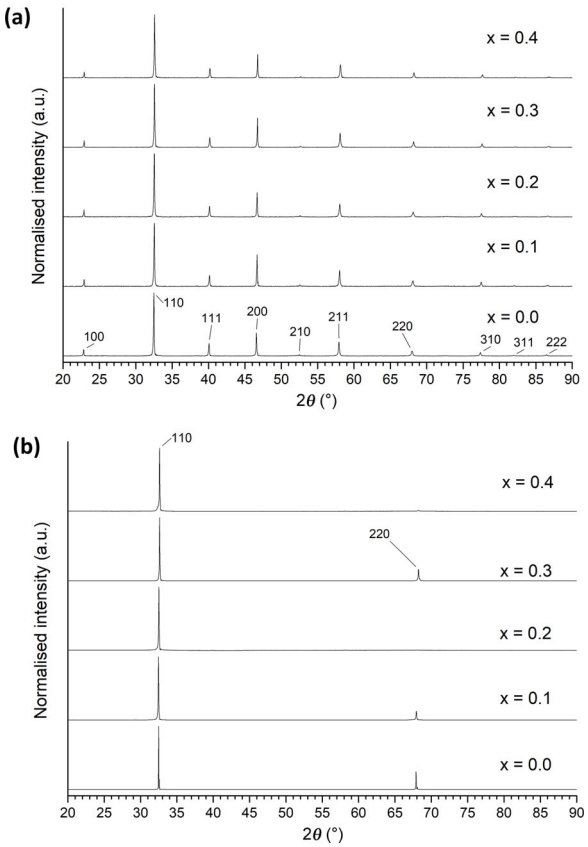

Fig. 2 XRD patterns of (a) $0.8(Na_{1/2}Bi_{1/2})TiO_3$–$0.2(Sr_{1-x}Ca_x)TiO_3$ polycrystalline ceramics sintered at 1200 ℃ for 1 h and (b) $0.8(Na_{1/2}Bi_{1/2})TiO_3$–$0.2(Sr_{1-x}Ca_x)TiO_3$ single crystals grown on (110) $SrTiO_3$ seed crystals at 1200 ℃ for 50 h.

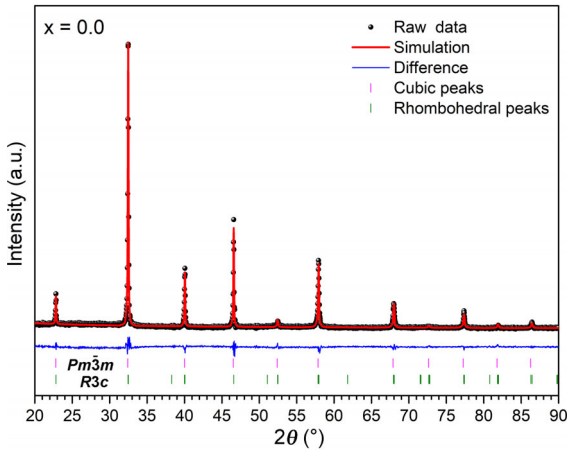

Fig. 3 Rietveld refinement of the XRD pattern of a $0.8(Na_{1/2}Bi_{1/2})TiO_3$–$0.2SrTiO_3$ polycrystalline ceramic sintered at 1200 ℃ for 1 h.

Table 1 Rietveld refinement results of $0.8(Na_{1/2}Bi_{1/2})TiO_3$–$0.2(Sr_{1-x}Ca_x)TiO_3$ polycrystalline ceramics sintered at 1200 ℃ for 1 h

x	$R3c$ phase (%)	$Pm\bar{3}m$ phase (%)	R_e	R_p	R_{wp}	χ^2
0.0	78.6	21.4	9.8	8.8	11.2	1.31
0.1	82.8	17.2	14.3	10.9	14.3	1.0024
0.2	85.3	14.7	13.9	10.7	13.9	1.012
0.3	87.9	12.1	9.8	8.5	11.2	1.31
0.4	90.1	9.9	13.9	10.7	13.9	1.0023

SEM micrographs of the calcined and ball-milled $0.8(Na_{1/2}Bi_{1/2})TiO_3$–$0.2(Sr_{1-x}Ca_x)TiO_3$ powders are shown in Fig. 4, along with their corresponding particle size distributions. The mean particle sizes of the powders vary from ~60 to 70 nm. The particle size distributions are quite broad, with some particles up to almost 400 nm in diameter. TEM micrographs of the calcined and ball-milled $0.8(Na_{1/2}Bi_{1/2})TiO_3$–$0.2(Sr_{1-x}Ca_x)TiO_3$ powders (x = 0.0 and 0.4) are shown in Fig. 5. The powder particles have a faceted shape. The powder particles were observed under two-beam conditions to check for the presence of dislocations. No dislocation loops are visible in the powder particles.

SEM micrographs of the $0.8(Na_{1/2}Bi_{1/2})TiO_3$–$0.2(Sr_{1-x}Ca_x)TiO_3$ single crystals grown on (001)-oriented $SrTiO_3$ seed crystals are shown in Fig. 6. Single crystal growth distance as a function of sintering time and composition is shown in Fig. 7(a). Data for the x = 0.0 composition is taken from Ref. [15]. Single crystals of all the compositions have grown epitaxially on the (001)-oriented $SrTiO_3$ seed crystals. The single crystal growth distance of all the samples

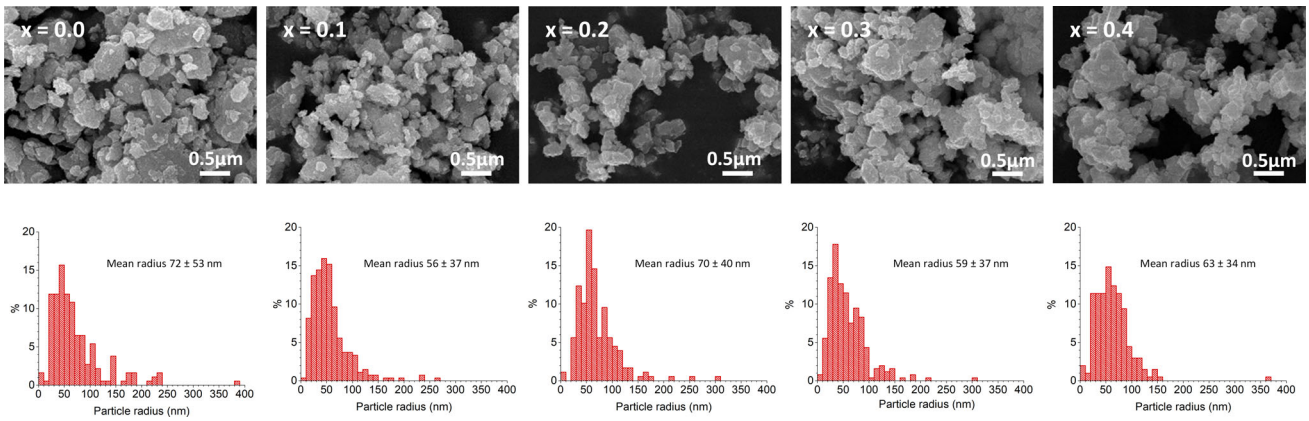

Fig. 4 SEM micrographs of calcined and ball-milled $0.8(Na_{1/2}Bi_{1/2})TiO_3$–$0.2(Sr_{1-x}Ca_x)TiO_3$ powders and their corresponding size distributions.

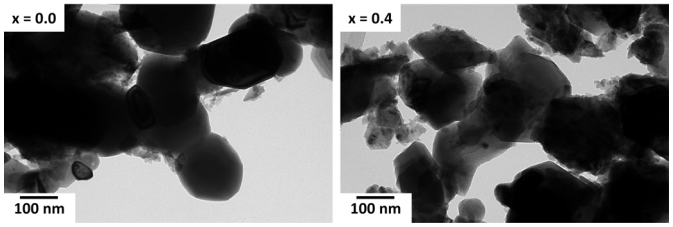

Fig. 5 TEM micrographs of calcined and ball-milled $0.8(Na_{1/2}Bi_{1/2})TiO_3$–$0.2(Sr_{1-x}Ca_x)TiO_3$ powders with $x = 0.0$ and $x = 0.4$.

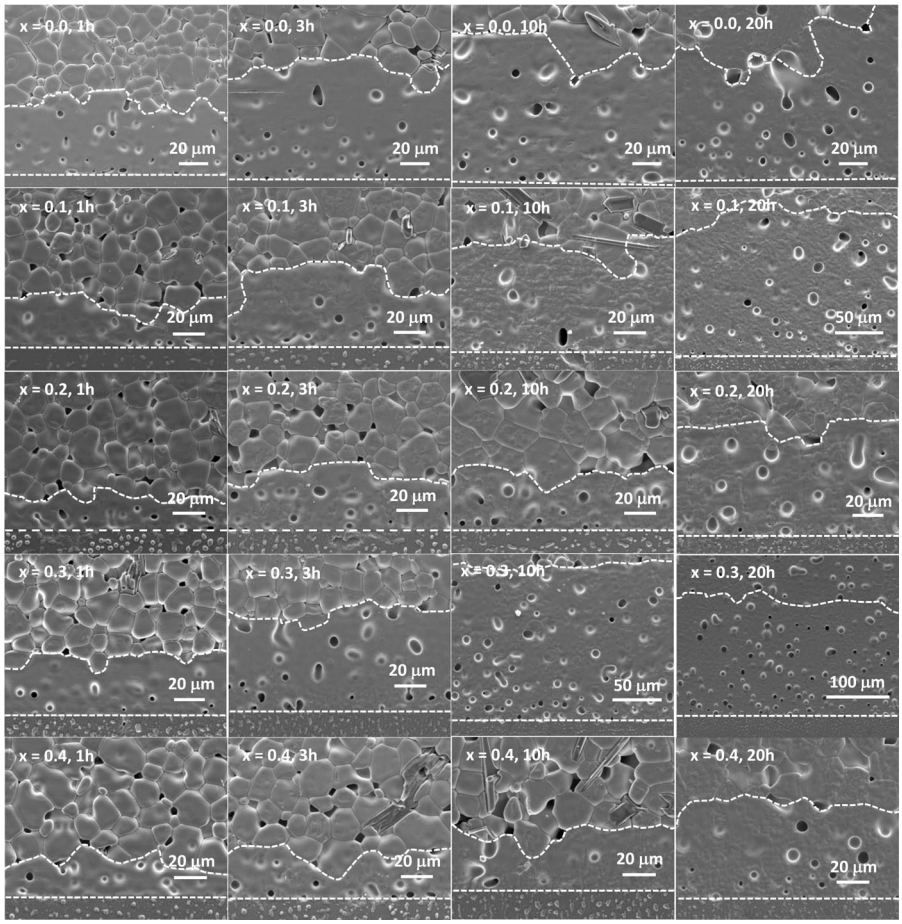

Fig. 6 SEM micrographs of $0.8(Na_{1/2}Bi_{1/2})TiO_3$–$0.2(Sr_{1-x}Ca_x)TiO_3$ single crystals grown on (001) $SrTiO_3$ seed crystals at 1200 ℃ for 1, 3, 10, and 20 h.

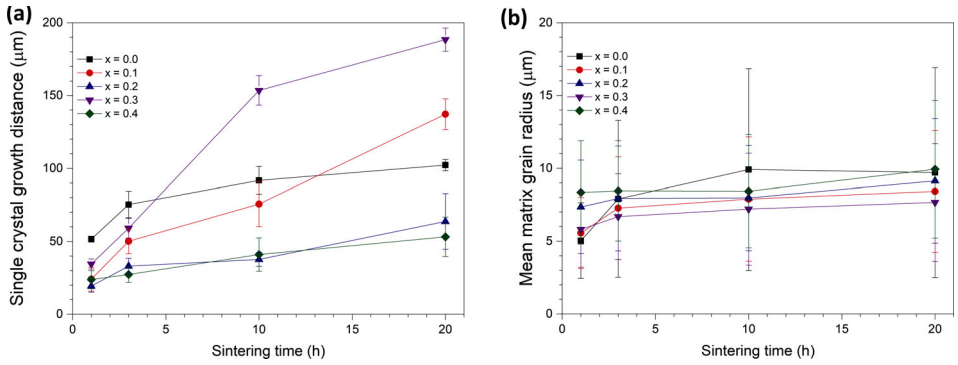

Fig. 7 (a) Single crystal growth distance of $0.8(Na_{1/2}Bi_{1/2})TiO_3$–$0.2(Sr_{1-x}Ca_x)TiO_3$ single crystals grown on (001) $SrTiO_3$ seed crystals at 1200 ℃ for 1, 3, 10, and 20 h; (b) mean matrix grain radius of the samples. Data for the x = 0.0 composition is taken from Ref. [15].

increases with sintering time. Single crystal growth distance tends to decrease with increasing Ca concentration from x = 0.0 from x = 0.4, except for samples with x = 0.3 which show anomalously high single crystal growth rates. The sample with x = 0.3 shows the largest single crystal growth distance of 188 μm after sintering for 20 h, whereas the sample with x = 0.4 shows the lowest growth distance of only 53 μm after sintering for the same time. All the single crystals are porous. A secondary phase appears to exist in the $SrTiO_3$ seed crystals. This may be an artefact caused by thermal etching [14]. Plate- and rod-shaped secondary phases are also visible in the matrix grains. EDS analysis of these secondary phases shows them to be TiO_2 and an Na_2O–TiO_2 compound, possibly $Na_2Ti_6O_{13}$. Peaks for these secondary phases were not visible in the XRD patterns of the sintered polycrystalline ceramics in Fig. 2(a), indicating that the amount of secondary phase is below the detection limit of the X-ray diffractometer.

SEM micrographs of the matrix grains are shown in Fig. 8. Mean matrix grain size as a function of sintering time and composition is shown in Fig. 7(b). Data for the x = 0.0 composition is taken from Ref. [15]. The grains are equiaxed, with larger grains appearing cubic in shape. The matrix is porous, as are the single crystals. Larger grains have pores trapped inside them. Secondary phases of TiO_2 and the same Na_2O–TiO_2 compound as in Fig. 7 are visible. For the samples with x = 0.0, the mean grain size increases with sintering time up to 10 h and then levels off. Substitution of Ca (x = 0.1) has little effect on mean grain size after 1 h of sintering, but causes a reduction in mean grain size and grain growth to level off after 3 h sintering. For the samples with x = 0.2 and x = 0.4, initial grain growth is rapid up to 1 h, after which grain growth is very sluggish. For the samples with x = 0.3, grain growth after 1 h is similar to that of the x = 0.0 and x = 0.1 samples. Further grain growth of the samples with x = 0.3 is reduced compared to all other compositions.

Grain size distributions of the matrix grains are shown in Fig. 9. Normalized grain size distributions (r/r_{mean}) are shown in Fig. 10. Data for the x = 0.0 composition is taken from Ref. [15]. For the x = 0.0 sample sintered for 1 h, the grain size distribution is relatively narrow, but some abnormal grains (defined as grains of size greater than three times the mean grain size [19]) are already present. As sintering time increases, the grain size distributions become broader and the number of abnormal grains increases. As the Ca content in the samples increases to x = 0.1, the grain size distributions become narrower and the number of abnormal grains decreases. Abnormal grain growth is on the verge of taking place after 3 h. For the samples with x = 0.2, the grain size distributions broaden again but from the normalized grain size distributions it is seen that no abnormal grains are present even after 20 h. For the samples with x = 0.3, the grain size distributions are narrow and abnormal grains appear after 3 h. For the samples with x = 0.4, the grain size distributions broaden again but again no abnormal grains are present.

Relative permittivity and loss tangent vs. temperature curves of the single crystal samples are shown in Fig. 11. All of the $0.8(Na_{1/2}Bi_{1/2})TiO_3$–$0.2(Sr_{1-x}Ca_x)TiO_3$ single crystals show a broad peak in relative permittivity without frequency dispersion at a temperature T_{max} and a shoulder at lower temperature T_s which shows frequency dispersion. Values of T_s and T_{max} are given in Table 2. T_{max} initially increases with replacement of Sr by Ca (x = 0.1 sample). Further substitution with Ca causes T_{max} to decrease (x = 0.2)

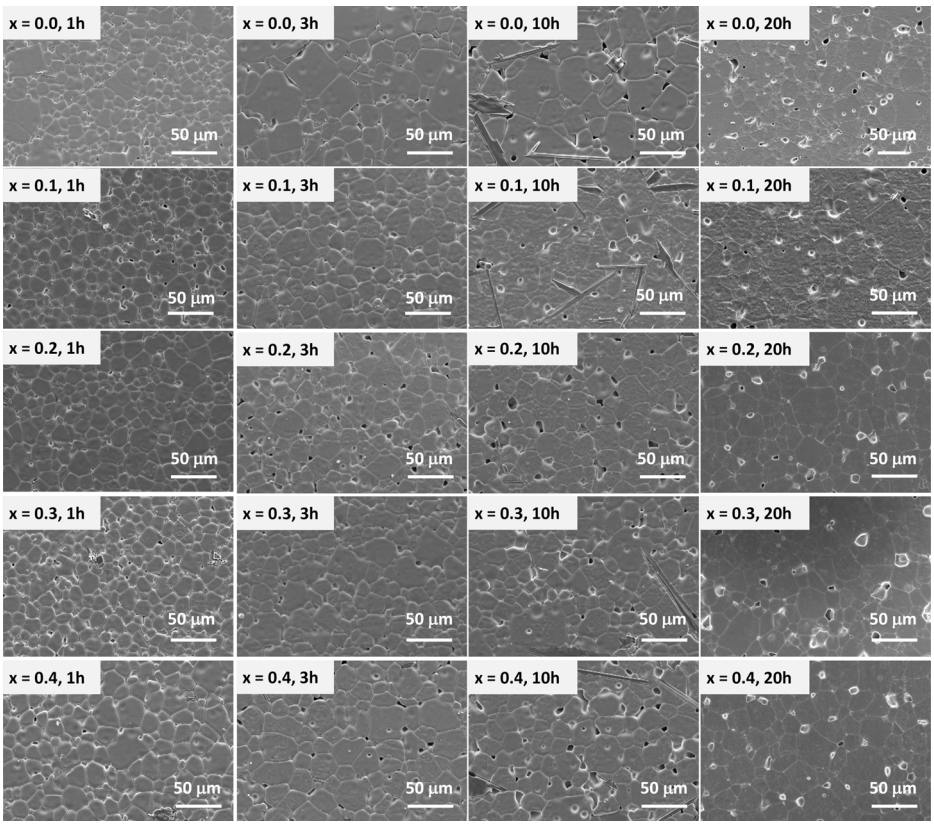

Fig. 8 SEM micrographs of $0.8(Na_{1/2}Bi_{1/2})TiO_3$–$0.2(Sr_{1-x}Ca_x)TiO_3$ matrix grains in samples sintered at 1200 ℃ for 1, 3, 10, and 20 h.

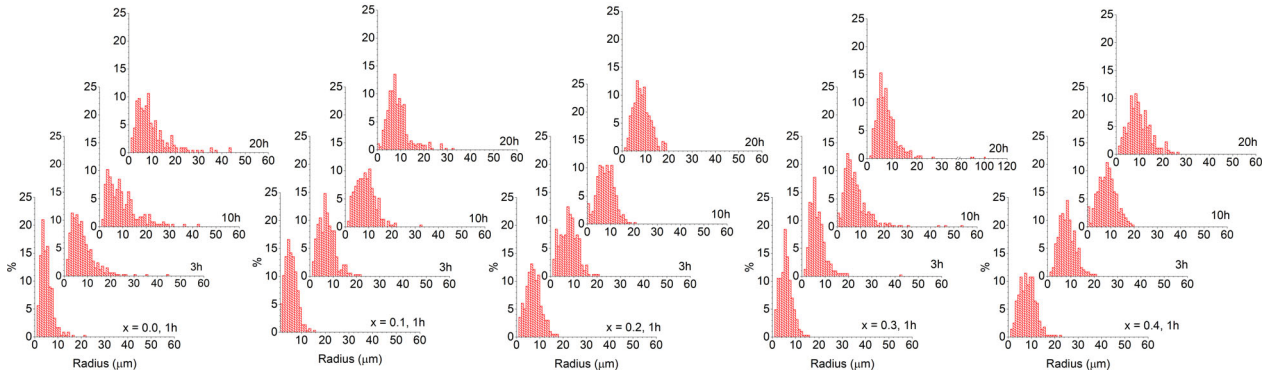

Fig. 9 Matrix grain size distributions of $0.8(Na_{1/2}Bi_{1/2})TiO_3$–$0.2(Sr_{1-x}Ca_x)TiO_3$ samples sintered at 1200 ℃ for 1, 3, 10, and 20 h. Data for the x = 0.0 composition is taken from Ref. [15].

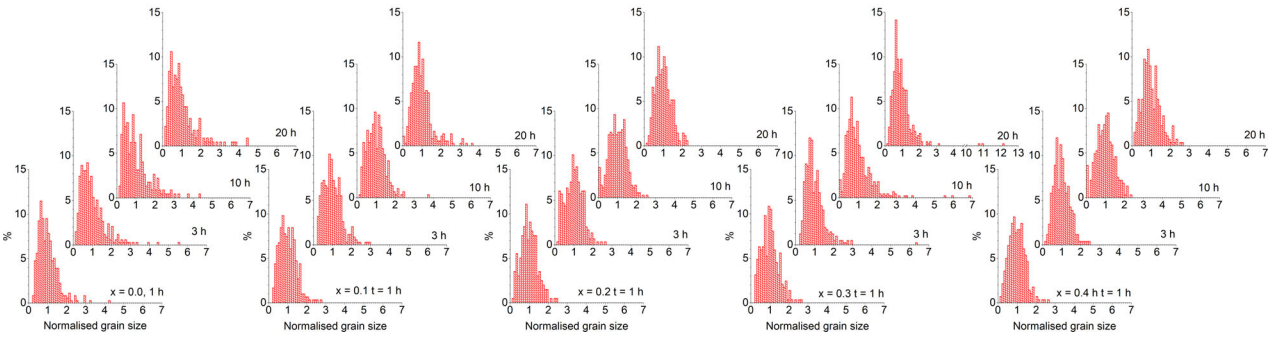

Fig. 10 Normalized matrix grain size distributions of $0.8(Na_{1/2}Bi_{1/2})TiO_3$–$0.2(Sr_{1-x}Ca_x)TiO_3$ samples sintered at 1200 ℃ for 1, 3, 10, and 20 h. Data for the x = 0.0 composition is taken from Ref. [15].

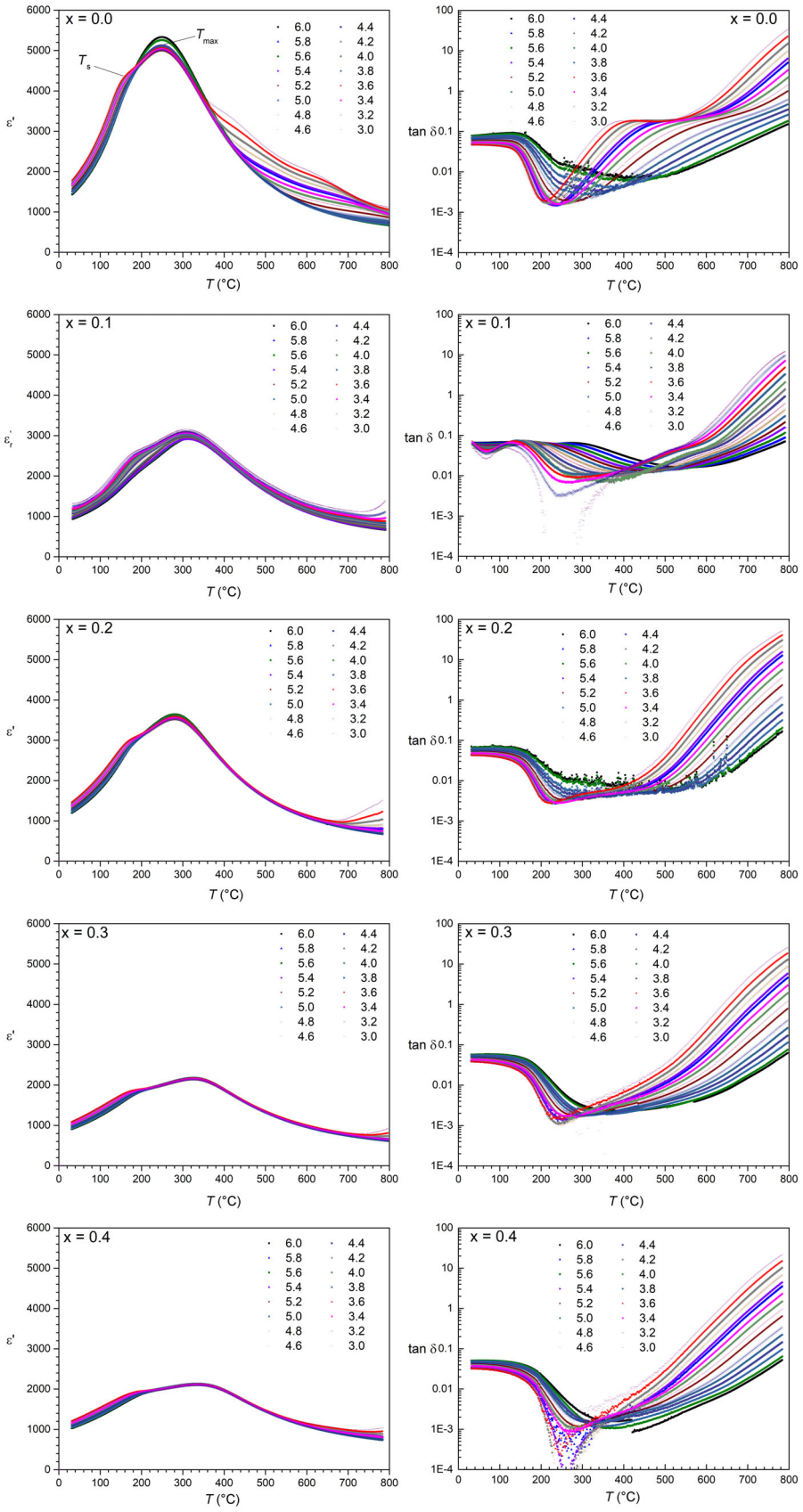

Fig. 11 Relative permittivity and loss tangent curves for $0.8(Na_{1/2}Bi_{1/2})TiO_3$–$0.2(Sr_{1-x}Ca_x)TiO_3$ single crystals grown on (110) $SrTiO_3$ seed crystals at 1200 ℃ for 50 h.

Table 2 T_s and T_{max} values of $0.8(Na_{1/2}Bi_{1/2})TiO_3$–$0.2(Sr_{1-x}Ca_x)TiO_3$ single crystals grown on (110) $SrTiO_3$ seed crystals at 1200 ℃ for 50 h

x	T_s (℃)	T_{max} (℃)
0.0	160	249
0.1	189	309
0.2	173	282
0.3	172	325
0.4	190	338

then increase again. T_s shows similar behaviour to T_{max}. Replacement of Sr with Ca causes relative permittivity values to generally decrease. The x = 0.0 curve shows increased frequency dispersion at temperatures above T_{max}. This may be caused by electrode polarization effects. The loss tangent vs. temperature curves show a peak corresponding to T_s and a minimum corresponding to T_{max}.

Figure 12 shows polarization vs. electric field (*PE*) curves of the $0.8(Na_{1/2}Bi_{1/2})TiO_3$–$0.2(Sr_{1-x}Ca_x)TiO_3$ single crystals. The x = 0.1 single crystal sample of thickness 83 μm was too thin to measure due to electrical breakdown. When the sample is very thin, open pores in the sample can cause a significant reduction in thickness and a large increase in the local electric field. This is exacerbated by the large pore size in the single crystals due to pore coalescence (Fig. 6) [7,20]. Values of saturation polarization P_{max}, remnant polarization P_r, and coercivity E_c are shown in Fig. 13(a). Replacement of Sr with Ca causes P_{max} to initially decrease and then increase again for x = 0.4. Remnant polarization P_r also initially decreases from x = 0.0 to x = 0.3 and then increases again for x = 0.4. Substitution of Sr with Ca causes E_c to initially remain almost constant for x = 0.2, decrease for x = 0.3, and then increase again for x = 0.4. The shape of the PE loop for the x = 0.2 sample is slightly asymmetric. The shape of the PE loops becomes pinched for the x = 0.3 and x = 0.4 samples.

Figure 12 also shows the bipolar strain vs. electric field (*SE*) curves of the $0.8(Na_{1/2}Bi_{1/2})TiO_3$–$0.2(Sr_{1-x}Ca_x)TiO_3$ single crystal samples as a function of the Ca concentration at 5 kV/mm electric field. The SE curve for the x = 0.0 sample has the typical butterfly shape of a normal ferroelectric material. Substitution of Sr with Ca causes S_{pos} to initially decrease for the x = 0.2 sample, followed by a small increase for the x = 0.3 and x = 0.4 samples. S_{neg} decreases

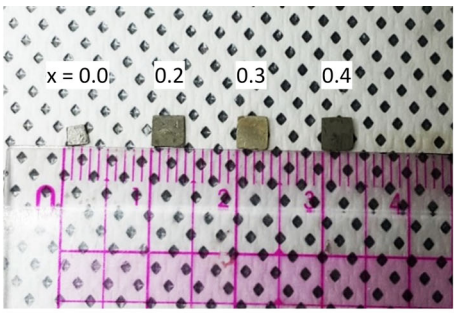

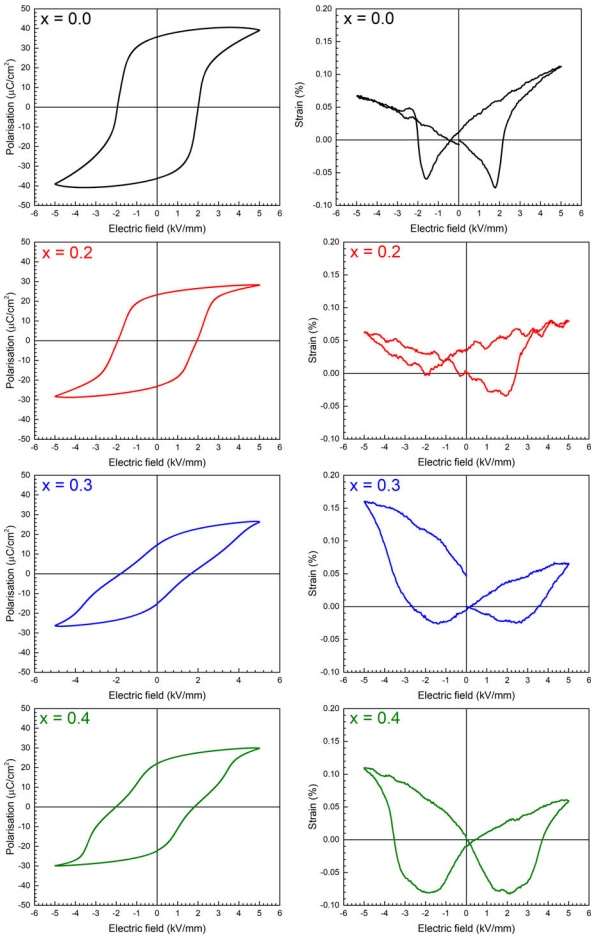

Fig. 12 Polarization vs. electric field loops and bipolar strain vs. electric field curves for $0.8(Na_{1/2}Bi_{1/2})TiO_3$–$0.2(Sr_{1-x}Ca_x)TiO_3$ single crystals grown on (110) $SrTiO_3$ seed crystals at 1200 ℃ for 50 h. The single crystal samples are also shown.

up to a value of x = 0.3 then increases again. The curves change shape from butterfly-shaped to sprout-shaped curves as Ca content increases to x = 0.3. As Ca content increases further to x = 0.4, the curve becomes more butterfly-shaped again with an increase in S_{neg}. Substitution of Sr with Ca initially causes a decrease in d^*_{33} (measured in the positive field direction) and an increase in strain hysteresis $\Delta S/S_{max}$, where ΔS is the

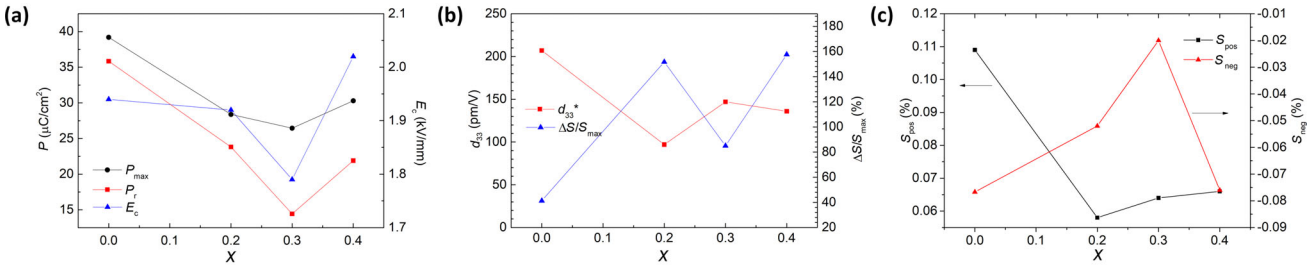

Fig. 13 (a) P_{max}, P_r, E_c, (b) d^*_{33}, $\Delta S/S_{max}$, and (c) S_{pos} and S_{neg} values of $0.8(Na_{1/2}Bi_{1/2})TiO_3$–$0.2(Sr_{1-x}Ca_x)TiO_3$ single crystals grown on (110) $SrTiO_3$ seed crystals at 1200 ℃ for 50 h.

difference in strain between the upper and lower parts of the curve when E = maximum positive electric field $E_{max}/2$ (x = 0.2) (Fig. 13(b)) [21]. Further substitution of Ca causes an increase in d^*_{33} whereas $\Delta S/S_{max}$ decreases and then increases again. The curves are asymmetrical, with higher S_{pos} values in the negative field direction for samples with x = 0.3 and x = 0.4. The crossover point of the curves does not pass through the origin. The gap between the start and finish of the curves for the x = 0.0 and x = 0.3 samples is an artifact caused by their small size.

4 Discussion

Initially, $(Na_{1/2}Bi_{1/2})TiO_3$ was determined to have a pseudocubic [22] or rhombohedral structure with *R*3*c* or *R*3*m* [23,24] space group at room temperature according to X-ray diffraction studies. The *R*3*c* space group was also favored by neutron diffraction studies [24]. Transmission electron microscopy studies, on the other hand, supported a coexistence of rhombohedral (*R*3*c*) and tetragonal (*P*4*bm* or $P4_2nm$) phases [25]. Recent high resolution X-ray diffraction studies proposed a monoclinic *Cc* space group [26], which was further supported by optical studies [27]. However, this assignment does not fully explain the $(Na_{1/2}Bi_{1/2})TiO_3$ structure and the room temperature phase may consist of *R*3*c* and *Cc* phases [28].

Formation of a solid solution with $SrTiO_3$ causes the structure to change from rhombohedral to pseudocubic as $SrTiO_3$ concentration in the NBT–ST system increases, with a morphotropic phase boundary (MPB) at x = 0.2–0.3 [4,5]. When Sr was substituted with Ca the fraction of rhombohedral phase increased (Table 1). This can be explained on the basis of the smaller ionic radius of Ca compared to Sr (0.134 nm vs. 0.144 nm for coordination number = 12) [29]. This causes a decrease in the Goldschmidt tolerance factor (using an ionic radius of 0.135 nm for Bi^{3+} with coordination number = 12 [30]) from 0.979 (x = 0.0) to 0.977 (x = 0.4). The MPB composition for binary $(Na_{1/2}Bi_{1/2})TiO_3$-based solid solutions appears for tolerance factors between 0.982 and 0.986 [30,31], with similar results for ternary systems [32,33]. Hence the decrease in tolerance factor as Sr is substituted with Ca moves the structure further into the rhombohedral phase field of the $(Na_{1/2}Bi_{1/2})TiO_3$–$SrTiO_3$ phase diagram.

Single crystal and matrix grain growth behaviour in the $0.8(Na_{1/2}Bi_{1/2})TiO_3$–$0.2(Sr_{1-x}Ca_x)TiO_3$ system is controlled by the structure of the interfaces between the grains, which can be disordered (rough) or ordered (smooth/faceted) on the atomic scale [34,35]. The structure of the grain interfaces in turn decides whether grain growth is controlled by diffusion of atoms between the shrinking and growing grains or by interface reaction at the surface of the growing grains. The faceted shape of the powder particles (Fig. 5) indicates that the interfaces will be ordered (faceted), as has been previously found in NBT-based systems [15,19,20]. The grain growth behaviour will then be controlled by interface reaction. For a system with solid/liquid interfaces, the driving force ΔG for grain growth of a particular grain is given by [36,37]:

$$\Delta G = 2\gamma V_m\left(\frac{1}{\bar{r}} - \frac{1}{r}\right) \quad (1)$$

where γ is the solid/liquid interfacial energy, r the radius of the grain, V_m the molar volume, and $\bar{r}$ the radius of the critical grain (a grain with ΔG = 0, i.e., that is neither growing nor shrinking). For a system where growth is controlled by diffusion, $\bar{r}$ is the mean grain radius r_{mean}, but for a system where growth is controlled by interface reaction, $\bar{r}$ is smaller than r_{mean} [37]. The seed crystal has $r >> \bar{r}$ and so the driving force for the single crystal is approximately [9]:

$$\Delta G = \frac{2\gamma V_m}{\bar{r}} \quad (2)$$

If the system has disordered interfaces, easy atom

attachment to or detachment from the surface of the grains means that the rate of atomic diffusion across the solid/liquid interface between the shrinking and growing grains limits grain growth [35,36]. The growth rate of any particular grain will increase linearly with its driving force (the dotted black line in Fig. 14(a)) and any grain with $\Delta G > 0$ can grow. In this case, the normalized size distribution of the grains (r / r_{mean}) is invariant with sintering time [35].

If the system has ordered interfaces, atoms that attach to the surface of the grain have a large number of broken bonds. They are unstable and will detach from the surface unless they can migrate to a favorable site such as a two-dimensional nucleus or a screw dislocation. The steps formed by such sites contain many kinks where atoms can attach without changing the interfacial energy of the grain [38]. The rate at which atoms can attach to the kink sites now limits grain growth, causing it to have a nonlinear relationship with driving force [37,39,40]. For a system where grain growth is controlled by the nucleation and growth of 2D nuclei, the rate of formation of stable 2D nuclei is very low below ΔG_c, the critical driving force. Grain growth is almost negligible because there are few kink sites available for atoms to attach to. At the critical driving force ΔG_c, the rate at which stable nuclei form increases exponentially. The grain can now grow because many kink sites are present. The grain growth rate therefore depends exponentially on ΔG (the dashed red line marked 2DNG in Fig. 14(a)) [41,42]. For $\Delta G > \Delta G_c$, kinetic roughening takes place [38,41,43]. Atoms can easily attach to the grain surface due to the presence of many nuclei, causing grain growth to become limited by diffusion. The grain growth rate is almost zero at $\Delta G < \Delta G_c$, increases exponentially at $\Delta G \approx \Delta G_c$ and then increases linearly with further increase in ΔG (the solid red line in Fig. 14(a)). Grains with $\Delta G < 0$ will shrink following a linear dependence with ΔG, as atoms can detach from each corner of the grain without increasing the grain's interfacial energy and multilayer dissolution can occur [35,36,39]. The value of ΔG_c for 2D nucleation-controlled growth is [35,39]:

$$\Delta G_c = \frac{\pi \varepsilon^2}{kTh} (\ln \psi n_0)^{-1} \tag{3}$$

where ε is the step free energy (the excess energy caused by the edge of the step), k is Boltzmann's constant, h is the step height of the 2D nucleus, and n_0 is the number density of atoms in the liquid. $\psi = n^* v \exp(\Delta g_m / kT)$, where n^* is the number of atoms in a position near to a critical 2D nucleus, v is the vibration frequency of atoms in the liquid, and Δg_m is the activation energy for jumping across the liquid/solid interface. ε varies with composition, dopant addition, sintering temperature, and atmosphere [44–46].

This type of grain growth behviour, interface-reaction limited below ΔG_c and diffusion-limited above ΔG_c, is known as mixed control growth. When grain growth is controlled by mixed control growth, the grain growth behaviour depends on the relative values of ΔG_c and ΔG_{max}, where ΔG_{max} is the maximum driving force for the largest grain in the system [35,36,47]. If $\Delta G_c \ll \Delta G_{max}$, a large number of grains have $\Delta G > \Delta G_c$ and can grow. As a result, the growth behaviour is similar to normal grain growth behaviour (pseudo-normal). If $\Delta G_c \approx \Delta G_{max}$, the grain growth is abnormal. Most of the matrix grains have $\Delta G < \Delta G_c$ and grow slowly or not at all. A small number of grains have $\Delta G \geqslant \Delta G_c$. These grains grow rapidly and can become much larger compared to other grains, becoming abnormal grains. If $\Delta G_c \gg \Delta G_{max}$, none of the grains can appreciably grow and grain growth is stagnant. In the solid state crystal growth method, the

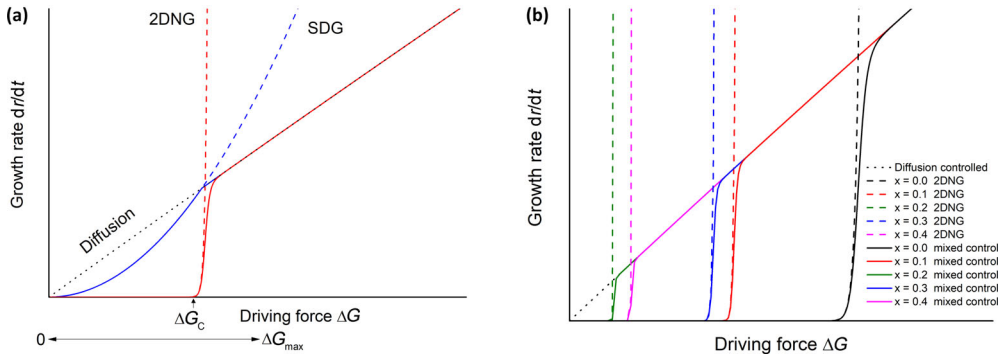

Fig. 14 (a) Schematic plot of growth rate vs. driving force for different types of grain growth; (b) schematic plot of growth rate vs. driving force for the $0.8(Na_{1/2}Bi_{1/2})TiO_3$–$0.2(Sr_{1-x}Ca_x)TiO_3$ compositions.

seed crystal behaves like an abnormal grain with driving force > ΔG_c [48–50]. A single crystal of the matrix composition grows on the seed crystal. Matrix grains that are large enough to have $\Delta G \geqslant \Delta G_c$ can also grow to form abnormal grains. The samples sintered in the present work were single phase and nominally free of a liquid phase. However, previous work in NBT-based compositions showed an amorphous phase at multi-grain junctions [15,19], indicating that a liquid phase may be present during sintering. Similar grain growth behaviour has also been found to occur during solid-state sintering [39,51–61].

Screw dislocations terminating at the grain surface form constantly regenerating ledges for easy atom attachment [40,43]. The grain growth rate then increases parabolically with ΔG (the dashed blue line marked SDG in Fig. 14(a)) [43]. The growth rate of the grain varies parabolically with ΔG for $\Delta G < \Delta G_c$ and linearly with ΔG for $\Delta G > \Delta G_c$ (the solid blue line in Fig. 14(a)). At $\Delta G > \Delta G_c$, kinetic roughening takes place as before and grain growth becomes diffusion controlled [40]. The difference in growth rate between grains with $\Delta G < \Delta G_c$ and grains with $\Delta G > \Delta G_c$ will be less drastic than in the case for 2D nucleation controlled growth.

The step free energy ε is important as its magnitude determines the value of ΔG_c and the grain growth behaviour. The magnitude of ε can be estimated from the macroscopic grain shape [62–64]. The grain shape in the $0.95(Na_{1/2}Bi_{1/2})TiO_3$–$0.05BaTiO_3$ system was found to be cubic with faceted {100} faces and rounded corners [19]. Our previous work on the NBT–ST system showed that the grains are cubic in shape, with flat faces and rounded edges and corners [15,20]. This indicates that NBT-based compositions have a moderate value of ε [62,64]. Grain growth behaviour in NBT-based systems tends to be initially pseudo-normal but changes to abnormal after extended sintering [15,19].

Figure 14(b) shows a schematic plot of growth rate vs. driving force for the $0.8(Na_{1/2}Bi_{1/2})TiO_3$–$0.2(Sr_{1-x}Ca_x)TiO_3$ compositions in the present work. Grain growth is assumed to be 2D-nucleation controlled growth due to the absence of screw dislocations (Fig. 5). From the particle size distributions in Fig. 4, it can be seen that the initial mean grain size is submicron for all the compositions and the particle size distributions are broad. The small values of r_{mean} indicates that the grains with $r > r_{mean}$ initially have a high driving force, as ΔG is inversely proportional to r_{mean} (Eq. (1) and Refs. [9,36]). For all the samples, at the beginning of sintering there are many grains with $\Delta G > \Delta G_c$ and so the matrix grain growth behaviour is initially pseudo-normal. For the sample with $x = 0.0$, as sintering proceeds the mean grain size r_{mean} increases, causing ΔG_{max} and ΔG for all the grains to decrease. As ΔG for a particular grain decreases, its growth rate decreases linearly. Once ΔG drops below ΔG_c, the growth rate for that grain no longer decreases linearly but exponentially. As the number of grains with $\Delta G > \Delta G_c$ decreases, the grain growth behaviour shifts from pseudo-normal to abnormal [19,36]. Most of the grains now have $\Delta G < \Delta G_c$ and are growing very slowly. A few grains have $\Delta G > \Delta G_c$ and can grow relatively quickly to form abnormal grains. For the samples with $x = 0.0$, this has begun to take place by 1 h. As sintering continues, both the normal grains and the abnormal grains continue to grow (very slowly and quickly, respectively) and the grain size distribution broadens and its peak shifts further to the right. The value of r_{mean} will level off with sintering time, as can be seen in Fig. 7(b).

The behaviour of the samples with $x = 0.1$ is consistent with a decrease in the step free energy ε. The value of the critical driving force ΔG_c shifts to the left (Fig. 14(b)). The value of ΔG_{max} is not affected, as this depends on the particle size distribution of the starting powder, which does not change much with composition (Fig. 4). The lower value of ΔG_c means that pseudo-normal grain growth can continue for longer before the driving force of most of the grains drops below ΔG_c and abnormal grain growth begins. Abnormal grain growth is just about to start after 3 h of sintering (Fig. 10). Because the value of ΔG_c is reduced, all the grains will have shifted to lower values of driving force and growth rate by the time that abnormal grain growth starts. Hence after abnormal grain growth starts, grain growth is more limited than in the case of the $x = 0.0$ samples. The matrix grain size remains smaller than in the case of the $x = 0.0$ samples and the grain size distributions remain narrower.

As Ca concentration increases to $x = 0.2$, step free energy ε decreases further and ΔG_c shifts to even lower values. Because the value of ΔG_c is very low, grain growth behaviour is pseudo-normal even up to 20 h. The grain size distribution changes slowly and retains a unimodal appearance. It is notable that the mean grain size after 1 h is larger than the $x = 0.0$ and $x = 0.1$ samples. This may be due to the larger number of grains

that have $\Delta G > \Delta G_c$ and are thus able to grow. For the samples with x = 0.3, the behaviour changes. The narrowing of the grain size distribution and the reappearance of abnormal grains after 3 h sintering indicate an increase in ε and ΔG_c. As Ca concentration increases further to x = 0.4, the grain size distributions broaden and grain growth is again pseudo-normal, indicating a decrease in ε and ΔG_c.

The seed crystal acts as an abnormal grain and a single crystal of the matrix composition grows on the seed during sintering. The driving force for growth of the single crystal is inversely proportional to the mean grain size (Eq. (2)) and will always be larger than ΔG_{max}, the driving force for growth of the largest matrix grain. For the x = 0.0 samples, pseudo-normal grain growth initially takes place in the matrix. Although the single crystal is also able to grow, it does not have a large advantage in growth rate over the matrix grains and so its growth will be limited [34]. Only when the driving force of most of the grains drops below ΔG_c will the single crystal have a significant growth advantage and grow rapidly. This corresponds with the start of abnormal grain growth in the matrix. From Fig. 7 and Fig. 9 it can be seen that this has happened by 1 h. As the mean matrix grain size increases with sintering time, the growth rate of the single crystal decreases, as can be seen in Fig. 7(a) for the x = 0.0 samples.

The crystal growth distance of the x = 0.1 sample is lower than that of the x = 0.0 sample, despite the fact that the mean matrix grain size is similar or smaller. This may be because the onset of abnormal grain growth is delayed to 3 h. During the pseudo-normal growth stage, the single crystal has to compete with a larger number of growing matrix grains for material from the shrinking grains, limiting its growth. By the time abnormal grain growth starts, the driving force for growth of the single crystal has shifted to a lower value than that of the x = 0.0 sample, reducing the growth rate of the single crystal even after abnormal grain growth starts. However, the small value of r_{mean} compared to the x = 0.0 samples allows the single crystal to continue growing even up to 20 h and eventually its growth distance overtakes that of the x = 0.0 sample. For the x = 0.2 samples, the large values of r_{mean} limit the single crystal growth rate. For the x = 0.3 samples, the small values of r_{mean} allow the single crystal to grow more rapidly than the other compositions due to its increased driving force for growth (Eq. (2)). For the x = 0.4 samples, the large values of r_{mean} limit single crystal growth, similar to the x = 0.2 samples.

The change in ε with change in composition is difficult to predict. The effect of solid solution formation on ε has been studied in several systems [34,46,65,66]. ε contains enthalpy h_s and entropy s_s terms and is given by $\varepsilon = h_s - Ts_s$ [64]. Substitution of Sr with Ca initially increases configurational entropy, causing an increase in s_s and a decrease in ε [67]. Composition changes also affect interatomic bond strengths and specific surface energies, further affecting ε. The decreased Ca–O bond strength (D^0_{298} = 383 kJ/mol) compared to Sr–O (D^0_{298} = 426 kJ/mol) [68] will decrease h_s, also causing a decrease in ε. Initially, substitution of Sr with Ca will decrease ε. Further addition of Ca has less effect on configurational entropy [67], causing the rate of decrease of ε to slow down. The reason for the apparent increase in ε for the x = 0.3 sample is not known.

All of the $0.8(Na_{1/2}Bi_{1/2})TiO_3$–$0.2(Sr_{1-x}Ca_x)TiO_3$ single crystals show behaviour typical of $(Na_{1/2}Bi_{1/2})TiO_3$-type ferroelectric relaxors, i.e., a broad peak in relative permittivity without frequency dispersion at a temperature T_{max} and a shoulder at lower temperature T_s which shows frequency dispersion [69–71]. The x = 0.0 sample shows a typical *PE* hysteresis loop for a normal ferroelectric material (Fig. 12). Similar to other NBT-based materials, the x = 0.0 sample at room temperature is in a non-ergodic relaxor state and can be transformed into a stable ferroelectric state by the electric field [70–72]. The sample then behaves like a normal ferroelectric material. The effect of Ca substitution on the dielectric and electromechanical behaviour of the single crystals appears contradictory at first sight. As Ca content increases from x = 0.0 to x = 0.3, the *PE* loops become increasingly pinched and the *SE* curves change from butterfly- to sprout-shaped (Fig. 12). This indicates that the material is changing from a non-ergodic relaxor to an ergodic relaxor and that Ca substitution is destabilizing the ferroelectric ordering of the material [73,74]. However, T_s and T_{max} also increase with Ca substitution (Fig. 11 and Table 2), which indicates the opposite. The origin of T_s is as yet unclear. It may be caused by a transition from the rhombohedral phase to tetragonal or mixed rhombohedral and tetragonal phases [24,75,76], thermal evolution of mixed rhombohedral and tetragonal polar nanoregions [70], a transition from non-ergodic to ergodic relaxor behaviour [77] or from a ferroelectric to relaxor ferroelectric state [78]. A decrease in T_s is

usually associated with the change of the bipolar strain hysteresis curves from butterfly to sprout-shaped and with the change from a non-ergodic to ergodic relaxor material [4,79,80]. However, in the present case T_s is increasing.

The change in the behaviour of the materials from a non-ergodic to ergodic relaxor material may be due to the reduction in tolerance factor caused by replacing Sr with Ca [81,82]. Reduction of the Goldschmidt tolerance factor destabilizes the non-ergodic ferroelectric behaviour [83]. The lower polarizability of Ca compared to Sr [1] may also weaken ferroelectric ordering in the material, making it easier for the electric field induced ferroelectric phase to return to an ergodic relaxor phase upon removal of the electric field, leading to a reduction in S_{neg}. The asymmetry of the *PE* loop for the $x = 0.2$ sample and the asymmetry of the *SE* curves may be caused by defects such as vacancies which pin the domain walls of the electric field induced ferroelectric phase [84]. Although the chemical composition of the crystals in this study was not measured, previous studies have shown that NBT-based single crystals grown by solid state crystal growth are Na deficient [15,20,85].

The piezoelectric properties of the $0.8(Na_{1/2}Bi_{1/2})TiO_3$–$0.2(Sr_{1-x}Ca_x)TiO_3$ single crystals are inferior to those of other NBT-based single crystals such as $(Na_{0.5}Bi_{0.5})TiO_3$–$BaTiO_3$ (d_{33}^* = 200–450 pm/V) [76,86] and $(Na_{0.5}Bi_{0.5})TiO_3$–$BaTiO_3$–$(K_{0.5}Na_{0.5})NbO_3$ (S_{pos} = 0.57%–0.9%) [21,87–90]. This may partially be because the $0.8(Na_{1/2}Bi_{1/2})TiO_3$–$0.2(Sr_{1-x}Ca_x)TiO_3$ single crystals have (110) orientation, which has relatively poor inverse piezoelectric properties in NBT-based single crystals [76,85,88,90]. It may also be due to the effect of Ca addition on the structure of the single crystals. From the Rietveld refinement results of the polycrystalline samples, it can be seen that replacing Sr with Ca increases the amount of rhombohedral phase in the material (Table 1). This is also consistent with the increase in T_s if T_s is assumed to be the temperature of transition from the rhombohedral phase to mixed rhombohedral and tetragonal phases (Fig. 11 and Table 2). This may explain the reduction in d_{33}^* and S_{pos} as Ca is substituted for Sr. Several workers have studied the electric field-induced phase transition in NBT-based materials. Hinterstein *et al.* [91] used *in-situ* X-ray and neutron diffraction techniques to study the electric field-induced phase transition in $0.92(Bi_{1/2}Na_{1/2})TiO_3$–$0.06BaTiO_3$–$0.02(K_{1/2}Na_{1/2})NbO_3$. They found a field-induced phase transition from a nonpolar pseudocubic (tetragonal) *P*4*bm* to a polar rhombohedral *R*3*c* phase. Chen *et al.* [90] studied the orientation dependence of the electric field-induced phase transition in single crystals of the same composition using *in-situ* Raman scattering and X-ray diffraction measurements. They found that application of the electric field in the [001] direction caused a phase transition from nonpolar tetragonal *P*4*bm* to polar tetragonal *P*4*mm*, with a corresponding large strain. Application of the electric field in the [111] direction however caused a partial transition to a rhombohedral phase with very little induced strain. Ge *et al.* [76] studied the electric field-induced phase transition of a $0.944(Bi_{1/2}Na_{1/2})TiO_3$–$0.056BaTiO_3$ single crystal at different temperatures. At temperatures close to T_s, an electric field induced phase transition from a nonpolar tetragonal *P*4*bm* phase to a polar tetragonal phase was observed, with a corresponding large electric field induced strain. From these studies it appears that the presence of a pseudocubic or a tetragonal *P*4*bm* phase is necessary to obtain large electric field induced strains in NBT-based single crystals. In the present work, replacing Sr with Ca reduces the amount of pseudocubic or tetragonal phase, thereby reducing the inverse piezoelectric properties.

5 Conclusions

The effect of replacing Sr with Ca on the matrix grain growth, single crystal growth, and electrical properties of $0.8(Na_{1/2}Bi_{1/2})TiO_3$–$0.2(Sr_{1-x}Ca_x)TiO_3$ single crystals (with x = 0.0–0.4) has been studied. An increase in the Ca content causes changes in matrix grain growth behaviour from abnormal to pseudo-normal behaviour, with an increase in mean matrix grain size and a corresponding reduction in single crystal growth. The $0.8(Na_{1/2}Bi_{1/2})TiO_3$–$0.2(Sr_{0.7}Ca_{0.3})TiO_3$ composition shows anomalous behaviour, with reduced mean matrix grain size and enhanced single crystal growth. XRD of polycrystalline samples shows them to contain mixed rhombohedral and cubic phases. Increasing Ca content causes an increase in the amount of rhombohedral phase. Increasing Ca content causes an increase in the shoulder temperature T_s and temperature of maximum relative permittivity T_{max} of the single crystals, a decrease in inverse piezoelectric properties, and a change from normal to incipient ferroelectric behaviour. This is likely due to the reduction of the

Goldschmidt tolerance factor and the increased amount of rhombohedral phase in the single crystals.

Acknowledgements

This research was supported by the Basic Science Research Program through the National Research Foundation of Korea (NRF), funded by the Ministry of Education under Grant No. 2015R1D1A1A01057060. Jong-Sook Lee acknowledges the support of the National Research Foundation (NRF) of Korea funded by the Ministry of Science and ICT (MSIT) (Grant No. NRF-2018R1A5A1025224).

The authors would like to thank Kyeong-Kap Jeong (Chonnam Centre for Research Facilities, Chonnam National University) for operating the XRD and Hey-Jeong Kim (Centre for Development of Fine Chemicals, Chonnam National University) for operating the SEM.

References

[1] Rödel J, Jo W, Seifert KTP, *et al*. Perspective on the development of lead-free piezoceramics. *J Am Ceram Soc* 2009, **92**: 1153–1177.

[2] Koruza J, Bell AJ, Frömling T, *et al*. Requirements for the transfer of lead-free piezoceramics into application. *J Materiomics* 2018, **4**: 13–26.

[3] Reichmann K, Feteira A, Li M. Bismuth sodium titanate based materials for piezoelectric actuators. *Materials* 2015, **8**: 8467–8495.

[4] Hiruma Y, Imai Y, Watanabe Y, *et al*. Large electrostrain near the phase transition temperature of $(Bi_{0.5}Na_{0.5})TiO_3$–$SrTiO_3$ ferroelectric ceramics. *Appl Phys Lett* 2008, **92**: 262904.

[5] Rout D, Moon KS, Kang SJL, *et al*. Dielectric and Raman scattering studies of phase transitions in the $(100–x)Na_{0.5}Bi_{0.5}TiO_3$–$xSrTiO_3$ system. *J Appl Phys* 2010, **108**: 084102.

[6] Acosta M, Jo W, Rödel J. Temperature- and frequency-dependent properties of the $0.75Bi_{1/2}Na_{1/2}TiO_3$–$0.25SrTiO_3$ lead-free incipient piezoceramic. *J Am Ceram Soc* 2014, **97**: 1937–1943.

[7] Lee D, Vu H, Sun HY, *et al*. Growth of $(Na_{0.5}Bi_{0.5})TiO_3$–$SrTiO_3$ single crystals by solid state crystal growth. *Ceram Int* 2016, **42**: 18894–18901.

[8] Sun HY, Fisher JG, Moon SH, *et al*. Solid-state-growth of lead-free piezoelectric $(Na_{1/2}Bi_{1/2})TiO_3$–$CaTiO_3$ single crystals and their characterization. *Mater Sci Eng: B* 2017, **223**: 109–119.

[9] Fisher JG, Benčan A, Godnjavec J, *et al*. Growth behaviour of potassium sodium niobate single crystals grown by solid-state crystal growth using $K_4CuNb_8O_{23}$ as a sintering aid. *J Eur Ceram Soc* 2008, **28**: 1657–1663.

[10] Krauss W, Schütz D, Mautner FA, *et al*. Piezoelectric properties and phase transition temperatures of the solid solution of $(1-x)(Bi_{0.5}Na_{0.5})TiO_3$–$xSrTiO_3$. *J Eur Ceram Soc* 2010, **30**: 1827–1832.

[11] Yi JY, Lee JK, Hong KS. Dependence of the microstructure and the electrical properties of lanthanum-substituted $(Na_{1/2}Bi_{1/2})TiO_3$ on cation vacancies. *J Am Ceram Soc* 2002, **85**: 3004–3010.

[12] Jo W, Ollagnier JB, Park JL, *et al*. CuO as a sintering additive for $(Bi_{1/2}Na_{1/2})TiO_3$–$BaTiO_3$–$(K_{0.5}Na_{0.5})NbO_3$ lead-free piezoceramics. *J Eur Ceram Soc* 2011, **31**: 2107–2117.

[13] Moon KS. Effect of Na_2CO_3 addition on grain growth behavior and solid-state single crystal growth in the $Na_{0.5}Bi_{0.5}TiO_3$–$BaTiO_3$ system. *J Korean Powder Metall Inst* 2018, **25**: 104–108.

[14] Lee DK, Vu H, Fisher JG. Growth of $(Na_{0.5}Bi_{0.5})TiO_3$–$Ba(Ti_{1-x}Zr_x)O_3$ single crystals by solid state single crystal growth. *J Electroceramics* 2015, **34**: 150–157.

[15] Le PG, Fisher JG, Moon WJ. Effect of composition on the growth of single crystals of $(1–x)(Na_{1/2}Bi_{1/2})TiO_3$–$xSrTiO_3$ by solid state crystal growth. *Materials* 2019, **12**: 2357.

[16] Han HS, Hong IK, Kong YM, *et al*. Effect of Nb doping on the dielectric and strain properties of lead-free $0.94(Bi_{1/2}Na_{1/2})TiO_3$–$0.06BaTiO_3$ ceramics. *J Korean Ceram Soc* 2016, **53**: 145–149.

[17] Cao J, Wang YF, Li Z. Effect of La doping on the electrical behaviors of BNT–BT based ceramics. *Ferroelectrics* 2017, **520**: 224–230.

[18] Praharaj S, Rout D, Kang SJL, *et al*. Large electric field induced strain in a new lead-free ternary $Na_{0.5}Bi_{0.5}TiO_3$–$SrTiO_3$–$BaTiO_3$ solid solution. *Mater Lett* 2016, **184**: 197–199.

[19] Moon KS, Kang SJL. Coarsening behavior of round-edged cubic grains in the $Na_{1/2}Bi_{1/2}TiO_3$–$BaTiO_3$ system. *J Am Ceram Soc* 2008, **91**: 3191–3196.

[20] Le PG, Jo GY, Ko SY, *et al*. The effect of sintering temperature and time on the growth of single crystals of $0.75(Na_{0.5}Bi_{0.5})TiO_3$–$0.25SrTiO_3$ by solid state crystal growth. *J Electroceramics* 2018, **40**: 122–137.

[21] Park JH, Kang SJL. Solid-state conversion of $(94-x)(Na_{1/2}Bi_{1/2})TiO_3$–$6BaTiO_3$–$x(K_{1/2}Na_{1/2})NbO_3$ single crystals and their enhanced converse piezoelectric properties. *AIP Adv* 2016, **6**: 015310.

[22] Smolenskii GA, Isupov VA, Agranovskaya AI, *et al*. New ferroelectrics of complex composition. *Soviet Physics Solid State* 1961, **2**: 2651–2654.

[23] Zvirgzds JA, Kapostin PP, Zvirgzde JV, *et al*. X-ray study of phase transitions in ferroelectric $Na_{0.5}Bi_{0.5}TiO_3$. *Ferroelectrics* 1982, **40**: 75–77.

[24] Jones GO, Thomas PA. Investigation of the structure and phase transitions in the novel A-site substituted distorted perovskite compound $Na_{0.5}Bi_{0.5}TiO_3$. *Acta Crystallogr Sect B* 2002, **58**: 168–178.

[25] Dorcet V, Trolliard G. A transmission electron microscopy study of the A-site disordered perovskite $Na_{0.5}Bi_{0.5}TiO_3$. *Acta Mater* 2008, **56**: 1753–1761.

[26] Gorfman S, Thomas PA. Evidence for a non-rhombohedral average structure in the lead-free piezoelectric material $Na_{0.5}Bi_{0.5}TiO_3$. *J Appl Crystallogr* 2010, **43**: 1409–1414.

[27] Gorfman S, Glazer AM, Noguchi Y, *et al*. Observation of a low-symmetry phase in $Na_{0.5}Bi_{0.5}TiO_3$ crystals by optical birefringence microscopy. *J Appl Crystallogr* 2012, **45**: 444–452.

[28] Rao BN, Fitch AN, Ranjan R. Ferroelectric-ferroelectric phase coexistence in $Na_{1/2}Bi_{1/2}TiO_3$. *Phys Rev B* 2013, **87**: 060102.

[29] Shannon RD. Revised effective ionic radii and systematic studies of interatomic distances in halides and chalcogenides. *Acta Crystallogr Sect A* 1976, **32**: 751–767.

[30] Hiruma Y, Nagata H, Takenaka T. Detection of morphotropic phase boundary of $(Bi_{1/2}Na_{1/2})TiO_3$–$Ba(Al_{1/2}Sb_{1/2})O_3$ solid-solution ceramics. *Appl Phys Lett* 2009, **95**: 052903.

[31] Hiruma Y, Nagata H, Takenaka T. Formation of morphotropic phase boundary and electrical properties of $(Bi_{1/2}Na_{1/2})TiO_3$–$Ba(Al_{1/2}Nb_{1/2})O_3$ solid solution ceramics. *Jpn J Appl Phys* 2009, **48**: 09KC08.

[32] Bai WF, Li LY, Li W, *et al*. Phase diagrams and electromechanical strains in lead-free BNT-based ternary perovskite compounds. *J Am Ceram Soc* 2014, **97**: 3510–3518.

[33] Bai W, Shen B, Zhai J, *et al*. Phase evolution and correlation between tolerance factor and electromechanical properties in BNT-based ternary perovskite compounds with calculated end-member $Bi(Me_{0.5}Ti_{0.5})O_3$ (Me = Zn, Mg, Ni, Co). *Dalton Trans* 2016, **45**: 14141–14153.

[34] Chung SY, Yoon DY, Kang SJL. Effects of donor concentration and oxygen partial pressure on interface morphology and grain growth behavior in $SrTiO_3$. *Acta Mater* 2002, **50**: 3361–3371.

[35] Kang SJL, Lee MG, An SM. Microstructural evolution during sintering with control of the interface structure. *J Am Ceram Soc* 2009, **92**: 1464–1471.

[36] Jung YI, Yoon DY, Kang SJL. Coarsening of polyhedral grains in a liquid matrix. *J Mater Res* 2009, **24**: 2949–2959.

[37] Park YJ, Hwang NM, Yoon DY. Abnormal growth of faceted (WC) grains in a (Co) liquid matrix. *Metall Mater Trans A* 1996, **27**: 2809–2819.

[38] Markov II. Crystal-ambient phase equilibrium. In: *Crystal Growth for Beginners: Fundamentals of Nucleation, Crystal Growth and Epitaxy*, 2nd edn. Singapore: World Scientific, 2003: 1–76.

[39] Kang SJL, Jung YI, Jung SH, *et al*. Interface structure-dependent grain growth behavior in polycrystals. In: *Microstructural Design of Advanced Engineering Materials*. Weinheim, Germany: Wiley-VCH Verlag GmbH & Co. KGaA, 2013: 299–322.

[40] Markov II. Crystal growth. In: *Crystal Growth for Beginners: Fundamentals of Nucleation, Crystal Growth and Epitaxy*, 2nd edn. Singapore: World Scientific, 2003: 181–351.

[41] Peteves SD, Abbaschian R. Growth kinetics of solid–liquid Ga interfaces: Part I. Experimental. *Metall Trans A* 1991, **22**: 1259–1270.

[42] Markov II. Nucleation. In: *Crystal Growth for Beginners: Fundamentals of Nucleation, Crystal Growth and Epitaxy*, 2nd edn. Singapore: World Scientific, 2003: 77–180.

[43] Peteves SD, Abbaschian R. Growth kinetics of solid–liquid Ga interfaces: Part II. Theoretical. *Metall Trans A* 1991, **22**: 1271–1286.

[44] Choi SY, Kang SJL. Sintering kinetics by structural transition at grain boundaries in barium titanate. *Acta Mater* 2004, **52**: 2937–2943.

[45] Zandvliet HJW, Gurlu O, Poelsema B. Temperature dependence of the step free energy. *Phys Rev B* 2001, **64**: 073402.

[46] Choi K, Hwang NM, Kim DY. Effect of grain shape on abnormal grain growth in liquid-phase-sintered $Nb_{1-x}Ti_xC$–Co alloys. *J Am Ceram Soc* 2002, **85**: 2313–2318.

[47] Fisher JG, Kang SJL. Strategies and practices for suppressing abnormal grain growth during liquid phase sintering. *J Am Ceram Soc* 2019, **102**: 717–735.

[48] Yang J, Yang QB, Li YX, *et al*. Growth mechanism and enhanced electrical properties of $K_{0.5}Na_{0.5}NbO_3$-based lead-free piezoelectric single crystals grown by a solid-state crystal growth method. *J Eur Ceram Soc* 2016, **36**: 541–550.

[49] Van Beijeren H. Exactly solvable model for the roughening transition of a crystal surface. *Phys Rev Lett* 1977, **38**: 993.

[50] Moon KS, Rout D, Lee HY, *et al*. Solid state growth of $Na_{1/2}Bi_{1/2}TiO_3$–$BaTiO_3$ single crystals and their enhanced piezoelectric properties. *J Cryst Growth* 2011, **317**: 28–31.

[51] Kizuka T. Atomic processes of grain-boundary migration and phase transformation in zinc oxide nanocrystallites. *Philos Mag Lett* 1999, **79**: 417–422.

[52] Lee BK, Chung SY, Kang SJL. Grain boundary faceting and abnormal grain growth in $BaTiO_3$. *Acta Mater* 2000, **48**: 1575–1580.

[53] Koo JB, Yoon DY. Abnormal grain growth in bulk Cu—The dependence on initial grain size and annealing temperature. *Metall Mater Trans A* 2001, **32**: 1911–1926.

[54] Merkle KL, Thompson LJ. Atomic-scale observation of grain boundary motion. *Mater Lett* 2001, **48**: 188–193.

[55] Merkle KL, Thompson LJ, Phillipp F. Collective effects in grain boundary migration. *Phys Rev Lett* 2002, **88**: 225501.

[56] Lee SB, Choi SY, Kang SJL, *et al*. TEM observations of singular grain boundaries and their roughening transition in TiO_2-excess $BaTiO_3$. *Zeitschrift Für Met* 2003, **94**: 193–199.

[57] Lee SB, Kim YM. Kinetic roughening of a Σ5 tilt grain boundary in $SrTiO_3$. *Acta Mater* 2009, **57**: 5264–5269.

[58] Lee SB, Kim YM, Ko DS, *et al*. Kinetic roughening of a ZnO grain boundary. *Appl Phys Lett* 2010, **96**: 191906.

[59] Fisher JG, Choi SY, Kang SJL. Influence of sintering atmosphere on abnormal grain growth behaviour in potassium sodium niobate ceramics sintered at low temperature. *J Korean Ceram Soc* 2011, **48**: 641–647.

[60] An SM, Yoon BK, Chung SY, *et al*. Nonlinear driving force-velocity relationship for the migration of faceted boundaries. *Acta Mater* 2012, **60**: 4531–4539.

[61] Lee SB, Yoo SJ, van Aken PA. Roughening of a stepped GaN grain boundary with increasing driving force for migration. *EPL Europhys Lett* 2017, **120**: 16002.

[62] Rottman C, Wortis M. Statistical mechanics of equilibrium crystal shapes: Interfacial phase diagrams and phase transitions. *Phys Rep* 1984, **103**: 59–79.

[63] Jo W, Hwang NM, Kim DY. Effect of crystal shape on the grain growth during liquid phase sintering of ceramics. *J Korean Ceram Soc* 2006, **43**: 728–733.

[64] Wortis M. Equilibrium crystal shapes and interfacial phase transitions. In: *Chemistry and Physics of Solid Surfaces VII*. Berlin, Heidelberg: Springer Berlin Heidelberg, 1988: 367–405.

[65] An SM, Kang SJL. Boundary structural transition and grain growth behavior in $BaTiO_3$ with Nd_2O_3 doping and oxygen partial pressure change. *Acta Mater* 2011, **59**: 1964–1973.

[66] Rheinheimer W, Altermann FJ, Hoffmann MJ. The equilibrium crystal shape of strontium titanate: Impact of donor doping. *Scripta Mater* 2017, **127**: 118–121.

[67] West AR. Crystal defects, non-stoichiometry and solid solutions. In: *Solid State Chemistry and its Applications*, 2nd edn. Chichester: John Wiley & Sons Ltd., 2014: 87–124.

[68] Luo YR. *Comprehensive Handbook of Chemical Bond Energies*. Boca Raton, FL: CRC Press, 2007.

[69] Shvartsman VV, Lupascu DC. Lead-free relaxor ferroelectrics. *J Am Ceram Soc* 2012, **95**: 1–26.

[70] Jo W, Schaab S, Sapper E, *et al*. On the phase identity and its thermal evolution of lead free $(Bi_{1/2}Na_{1/2})TiO_3$–6 mol% $BaTiO_3$. *J Appl Phys* 2011, **110**: 074106.

[71] Liu G, Dong J, Zhang LY, *et al*. Phase evolution in $(1-x)(Na_{0.5}Bi_{0.5})TiO_3$–$xSrTiO_3$ solid solutions: A study focusing on dielectric and ferroelectric characteristics. *J Materiomics* 2020, **6**: 677–691.

[72] Weyland F, Acosta M, Vögler M, *et al*. Electric field-temperature phase diagram of sodium bismuth titanate-based relaxor ferroelectrics. *J Mater Sci* 2018, **53**: 9393–9400.

[73] Jo W, Dittmer R, Acosta M, *et al*. Giant electric-field-induced strains in lead-free ceramics for actuator applications—Status and perspective. *J Electroceramics* 2012, **29**: 71–93.

[74] Liu X, Shen B, Zhai JW. Designing novel sodium bismuth titanate lead-free incipient perovskite for piezoactuator applications. *J Am Ceram Soc* 2019, **102**: 6751–6759.

[75] Tu CS, Huang SH, Ku CS, *et al*. Phase coexistence and Mn-doping effect in lead-free ferroelectric $(Na_{1/2}Bi_{1/2})TiO_3$ crystals. *Appl Phys Lett* 2010, **96**: 062903.

[76] Ge WW, Luo CT, Zhang QH, *et al*. Ultrahigh electromechanical response in $(1–x)(Na_{0.5}Bi_{0.5})TiO_3$–$x BaTiO_3$ single-crystals via polarization extension. *J Appl Phys* 2012, **111**: 093508.

[77] Lee HY, Wang K, Yao FZ, *et al*. Identifying phase transition behavior in $Bi_{1/2}Na_{1/2}TiO_3$–$BaTiO_3$ single crystals by piezoresponse force microscopy. *J Appl Phys* 2017, **121**: 174103.

[78] Craciun F, Galassi C, Birjega R. Electric-field-induced and spontaneous relaxor-ferroelectric phase transitions in $(Na_{1/2}Bi_{1/2})_{1-x}Ba_xTiO_3$. *J Appl Phys* 2012, **112**: 124106.

[79] Hiruma Y, Nagata H, Takenaka T. Phase diagrams and electrical properties of $(Bi_{1/2}Na_{1/2})TiO_3$-based solid solutions. *J Appl Phys* 2008, **104**: 124106.

[80] Wang K, Hussain A, Jo W, *et al*. Temperature-dependent properties of $(Bi_{1/2}Na_{1/2})TiO_3$–$(Bi_{1/2}k_{1/2})TiO_3$–$SrTiO_3$ lead-free piezoceramics. *J Am Ceram Soc* 2012, **95**: 2241–2247.

[81] Han HS, Ahn CW, Kim IW, *et al*. Destabilization of ferroelectric order in bismuth perovskite ceramics by A-site vacancies. *Mater Lett* 2012, **70**: 98–100.

[82] Ishchuk VM, Kuzenko DV, Sobolev VL. Dimensional *t*-factor variation and increase of stability of the ferroelectric state in $(Na_{0.5}Bi_{0.5})TiO_3$-based solid solutions. *J Adv Dielec* 2017, **7**: 1750030.

[83] Lee JK, Hong KS, Kim CK, *et al*. Phase transitions and dielectric properties in A-site ion substituted $(Na_{1/2}Bi_{1/2})TiO_3$ ceramics (A = Pb and Sr). *J Appl Phys* 2002, **91**: 4538.

[84] Jin L, Li F, Zhang S. Decoding the fingerprint of ferroelectric loops: Comprehension of the material properties and structures. *J Am Ceram Soc* 2014, **97**: 1–27.

[85] Le PG, Pham TL, Nguyen DT, *et al*. Solid state crystal growth of single crystals of $0.75(Na_{1/2}Bi_{1/2})TiO_3$–$0.25SrTiO_3$ and their characteristic electrical properties. *J Asian Ceram Soc* 2021, **9**: 63–74.

[86] Luo C, Ge W, Zhang Q, *et al*. Crystallographic direction dependence of direct current field induced strain and phase transitions in $Na_{0.5}Bi_{0.5}TiO_3$–$x\%BaTiO_3$ single crystals near the morphotropic phase boundary. *Appl Phys Lett* 2012, **101**: 141912.

[87] Wang YJ, Luo CT, Wang SH, *et al*. Large piezoelectricity in ternary lead-free single crystals. *Adv Electron Mater* 2020, **6**: 1900949.

[88] Park JH, Lee HY, Kang SJL. Solid-state conversion of $(Na_{1/2}Bi_{1/2})TiO_3$–$BaTiO_3$–$(K_{1/2}Na_{1/2})NbO_3$ single crystals and their piezoelectric properties. *Appl Phys Lett* 2014, **104**: 222910.

[89] Chen C, Zhao XY, Wang YJ, *et al*. Giant strain and electric-field-induced phase transition in lead-free $(Na_{0.5}Bi_{0.5})TiO_3$–$BaTiO_3$–$(K_{0.5}Na_{0.5})NbO_3$ single crystal. *Appl Phys Lett* 2016, **108**: 022903.

[90] Chen C, Wang YJ, Jiang XP, *et al*. Orientation dependence of electric field induced phase transitions in lead-free $(Na_{0.5}Bi_{0.5})TiO_3$-based single crystals. *J Am Ceram Soc* 2019, **102**: 4306–4313.

[91] Hinterstein M, Knapp M, Hölzel M, *et al*. Field-induced phase transition in $Bi_{1/2}Na_{1/2}TiO_3$-based lead-free piezoelectric ceramics. *J Appl Crystallogr* 2010, **43**: 1314–1321.